Journal of Structural Geology 31 (2009) 29–43

Contents lists available at ScienceDirect

Journal of Structural Geology

journal homepage: www.elsevier.com/locate/jsg

Dehydration and deformation of intact cylinders of serpentinite

E.H. Rutter*, S. Llana-Fúnez [1], K.H. Brodie

Rock Deformation Laboratory, School of Earth, Atmospheric and Environmental Sciences, University of Manchester, Manchester M13 9PL, UK

ARTICLE INFO

Article history:
Received 24 February 2008
Received in revised form 11 August 2008
Accepted 30 September 2008
Available online 17 October 2008

Keywords:
Deformation/metamorphism
Experimental rock deformation
Serpentinite dehydration
Porosity collapse

ABSTRACT

Experimental deformation of intact lizardite serpentinite samples was carried out to study the effect of the dehydration reaction to olivine + talc + water under controlled pore water pressure. The dehydration reaction dramatically increases the porosity of the sample, causing weakening, but progressive pore collapse during deformation leads to strain-hardening. The concepts of critical state soil mechanics can be used to describe the overall behaviour of the porous material. At low strain rates, a transition to linear-viscous flow was observed and inferred to be due to the formation of fine-grained olivine in the dehydration reaction. The resultant inability of the rock to support high loads during dehydration at low strain rates means that the production of high pressure water by dehydration and its subsequent expulsion will favour seismogenic failure in the surrounding rocks not directly involved in the dehydration reaction, rather than the serpentinite itself.

1. Introduction

The strength and ductility (deformability) of rocks in nature are believed to be strongly influenced by metamorphic reactions, especially when fluids are evolved and volume changes occur. Apart from the effects of growth of new mineral phases whose mechanical strength might be intrinsically different from that of pre-existing phases, mechanical interactions between deformation and metamorphic reactions include (a) changes in the effective stress state through the evolution of fluid under pressure (e.g. H_2O or CO_2) in the case of devolatilization reactions (e.g. Raleigh and Paterson, 1967; Olgaard et al., 1995), (b) changes to point defect chemistry of minerals (e.g. quartz) arising from changes in the activity of components of the fluid phase (e.g. Rutter and Brodie, 2004), (c) formation of reaction products sufficiently fine-grained to provoke a change in deformation mechanism to grain-size sensitive flow (e.g. Rutter and Brodie, 1988; Drury, 2005; de Ronde et al., 2005), (d) enhancement of intracrystalline plastic deformation through stresses arising from solid phase volume changes (e.g. Poirier, 1982), (e) weakening and enhancement of ductility through formation of new porosity (Rutter and Brodie, 1995).

Serpentinites are well-suited to the study of deformation/metamorphism relations because the rock is initially strong yet can undergo substantial changes in mechanical properties in association with its dehydration reaction (Raleigh and Paterson, 1967; Rutter and Brodie, 1988; Miller et al., 2003; Jung et al., 2004; Hirose et al., 2006; Arkwright et al., 2008). It is also an important reaction in its own right because it is believed to play a key role in seismogenesis in subduction zones and in oceanic transform faults. The dehydration of serpentinite (variety lizardite) occurs in the laboratory over the temperature range 500–580 °C (e.g. Llana-Fúnez et al., 2007), over a period from a few days to a few hours.

In a previous study we used porous, isostatically hot-pressed powder samples in order to ensure control over pore fluid pressure through guaranteed connectivity of the pores spaces of the specimen with the pore pressure system outside of the pressure vessel (Arkwright et al., 2008). However, Tenthorey and Cox (2003) showed that the dehydration of intact, initially zero-porosity serpentinite led rapidly to the development of sufficient permeability to ensure that a specimen would be sufficiently drained, and this conclusion has also been confirmed by our studies on intact samples reported here. Samples were deformed under drained conditions with constant pore water pressure, preventing the build-up of high pore fluid pressures, so that we could specifically study the influence on deformability of the arrangement of new olivine grains and the distribution of porosity. In almost all experiments, pore volumometry was used, enabling tracking of volume changes during the dehydration and deformation phases when they were carried out sequentially. If the two processes contribute to volume change at the same time, their individual contributions to volume change cannot be separated.

Samples were deformed at different temperatures, (a) before reaction onset, (b) during the course of the reaction, and (c) after the reaction had gone to completion, over a range of strain rates, in

* Corresponding author.
E-mail address: e.rutter@manchester.ac.uk (E.H. Rutter).
[1] Present address: Earth and Ocean Sciences, University of Liverpool, Liverpool L69 3GP, UK.

0191-8141/$ – see front matter © 2008 Elsevier Ltd. All rights reserved.
doi:10.1016/j.jsg.2008.09.008

order to study the effect of the dehydration reaction on strength and ductility.

2. Experimental details

2.1. Sample material

The starting material for sample fabrication was a fully serpentinized dunite (Fig. 1a) collected from Porthallow, in the Lizard ophiolitic complex of SW England. The modal composition of the rock (vol %) was estimated from element mapping in the scanning electron microscope (SEM) to be lizardite (serpentine) $92 \pm 3\%$, clinochlore $4.3 \pm 2.1\%$, magnetite $3.5 \pm 1.6\%$ and Cr spinel $<0.5\%$. The porosity of the starting material was determined by gravimetric methods to be less than 0.1%. Microstructurally, the rock is a uniformly mesh-textured serpentinite in which serpentine pseudomorphs original olivine crystals 50–100 μm across, with old grain boundaries and cracks highlighted as veinlets of serpentinite that accommodated the excess volume produced during serpentinization (Fig. 1a). The minor amount of chlorite is sometimes hard to distinguish in the SEM from the serpentine phase, but brightly contrasting oxide grains and grain clusters up to 30 μm across occur

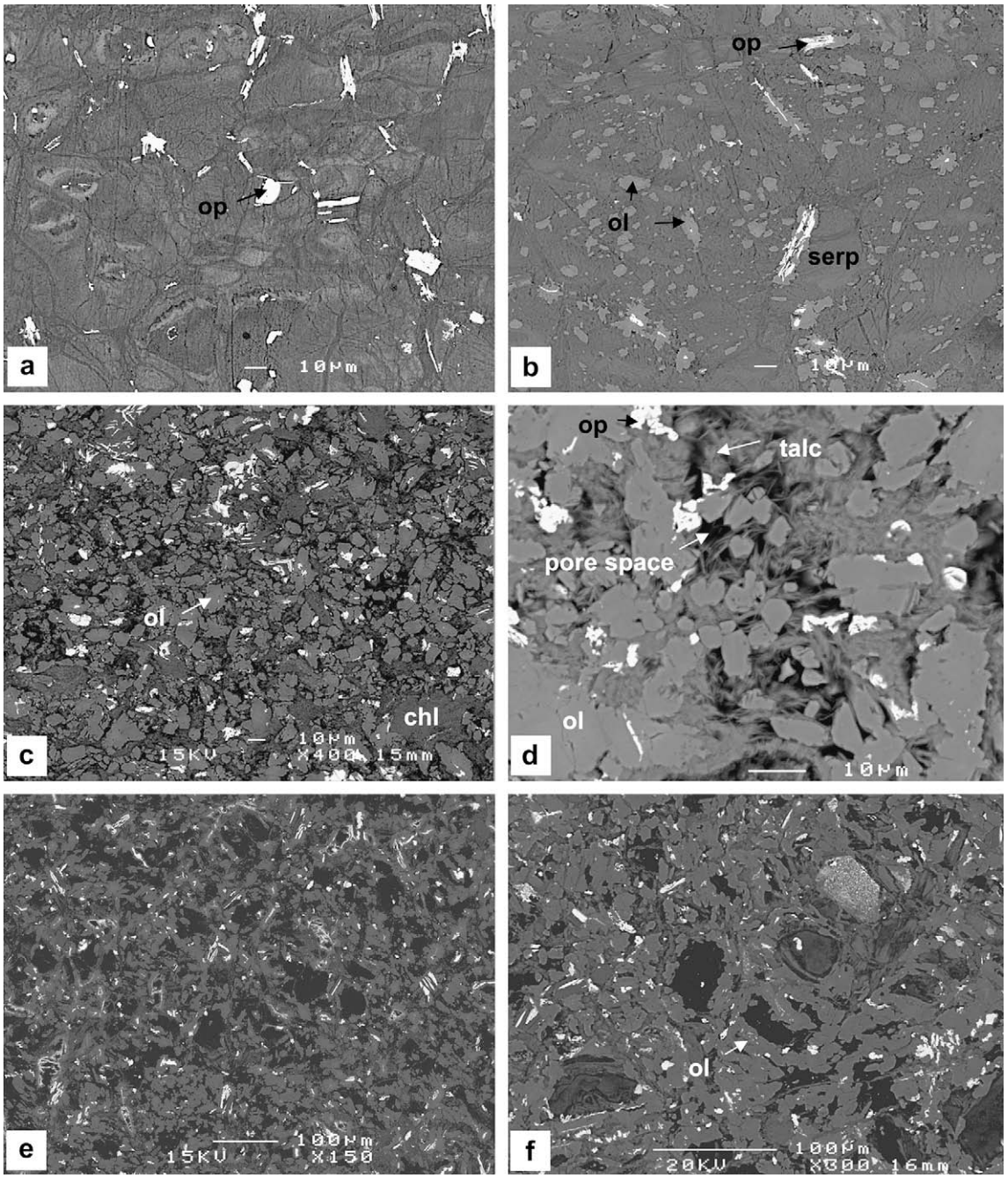

Fig. 1. SEM backscattered electron micrographs showing: (a) serpentinite starting material. Variation in grey levels reflects small variations in Fe within the serpentine. Op = oxide phase (bright). (b) Sample after partial dehydration showing small olivine grains (ol) nucleating randomly and on some Fe oxides (sample 63). (c) Near-full dehydration under low effective pressure showing development of olivine and talc and the formation of porosity (black areas) (sample 6). (d) Higher magnification image showing growth of euhedral olivines (ol), talc plates and porosity generation by the reaction (sample 98). (e) Dehydration under higher effective pressure tends to result in a growth of new olivine along original grain boundaries in the serpentinite, producing a cellular structure (sample 16). (f) Higher magnification showing the development of a framework of olivine grains (sample 77).

scattered throughout the matrix and along the central parts of serpentine veinlets and old olivine grain boundaries. Minor compositional variation and zoning of Fe–Mg in serpentine are shown by variation in grey levels in backscattered electron images.

2.2. Experimental methodology

Experiments were performed using an externally heated 'Nimonic' testing machine (named for the nickel-based alloy from which the pressure vessel is fabricated), capable of operation for indefinite periods at temperatures up to 700 °C and confining and pore fluid pressures up to 250 MPa. Cylindrical specimens (9.4 mm in diameter) were cored from a block of serpentinite and cut and ground to a length of 22 mm. They were deformed in annealed copper jackets of 0.25 mm wall thickness. Constant pore pressure was applied to the sample via a hollow loading piston that also carried an inconel-sheathed thermocouple. Specimen temperature variations along the sample length were typically less than 4 °C. Axial load was measured using a semi-internal load cell with a load resolution (in terms of differential stress on the specimen) of better than 1 MPa.

When porosity formed as a result of the dehydration reaction collapses during deformation, the cross-sectional area of the specimen is reduced, which increases the differential stress corresponding to a given differential load. This tends to offset the increase in cross-sectional area that normally occurs with progressive strain in an isovolumetric sample during axisymmetric loading. Pore volumometer data (see below) were used to correct for this effect, assuming the volume change is applied homogeneously throughout the specimen. Differential stresses were also corrected for the strength of the copper jacket (typically equivalent to ca 2–10 MPa differential stress on the specimen according to load, temperature, strain and strain rate).

Pore water pressure was controlled by means of a pore volumometer, in which a piston can be driven into a small volume (3 cm^3) pressure vessel via a DC servo-motor, which in turn can be used to maintain pore water pressure constant via feedback from the pore pressure transducer. In this mode of operation, displacements of the piston measure changes in the volume of the volumometer cylinder to a resolution of ca 0.15 mm^3 at room temperature. Thus after correction for the difference in specific volume of water at the test temperature relative to room temperature, the progression of the dehydration reaction or fluid expulsion due to pore collapse can be measured.

Pore volumometry is a method widely used for low temperature studies on porous rocks, but has not received much application at high temperatures (e.g. Renner et al., 2003). We have previously used pore volumometry to study the kinetics of this dehydration reaction as a function of temperature and effective pressure (Llana-Fúnez et al., 2007). Pore volumometry above the critical temperature of water is most reliable at pore pressures of at least 50 MPa. At lower pressures the specific volume of water increases greatly, which decreases the sensitivity of the volumometer measurement. Additionally, pressure fluctuations due to convective refluxing in the hollow upper loading piston causes short-term pressure fluctuations. As the volumometer servo-system tries to follow them they are converted into apparent volume fluctuations that appear as noise.

Reaction progress can be measured at a given temperature provided the effective pressure on the sample is not enough to cause pore collapse. Conversely, during deformation, the pore volumometer measures compaction of pore space produced in the reaction, provided (a) temperature has been lowered sufficiently to stop the reaction (in the present case by lowering the temperature to 450 °C), or (b) if the reaction is known to have gone to completion, or (c) if the deformation temperature is such that the duration of the deformation is short compared to the time required for complete dehydration. Use of initially intact samples of the near-zero-porosity rock ensured that porosity changes could only occur due to the dehydration reaction or to subsequent pore collapse or dilatation.

The following sets of deformation experiments were performed:

(a) constant displacement rate tests over a range of displacement rates,
  (i) prior to dehydration (at 450 °C) both wet and dry,
  (ii) during dehydration (in the temperature range 520–570 °C) such that the dehydration reaction would take place over approximately the same or a longer time interval as the deformation, and
  (iii) samples dehydrated completely over a period of 24 h at 560 °C, followed by cooling to 450 °C to ensure the reaction was stopped. Experiments were carried out over a range of effective confining pressure. In these tests, pore volumometry only measures pore volume changes associated with deformation.
  (iv) Talc is a volumetrically significant reaction product in these dehydration experiments and is known to be relatively weak. To evaluate its possible contribution to controlling the strength of the dehydrated samples, several tests were run on cylinders of high-purity, polycrystalline talc, both wet and dry (material supplied by the Dunlop Rubber company). The rock consists of almost 100% talc, of near-zero porosity. Grains are up to 10 μm long and less than 1 μm wide, with no apparent preferred orientation.
(b) Strength sensitivity to strain rate was further evaluated through stress-stepping and stress-relaxation tests to attain slower strain rates than normally accessible in constant displacement rate tests.

2.3. Microstructural observations

Microstructural studies of hot-pressed and deformed samples were made by SEM on polished surfaces, and by transmission electron microscopy (TEM) on thin foils prepared by ion beam milling. Changes in modal proportion of olivine were used to estimate the amount of dehydration reaction at the end of a test from backscattered electron (BSE) images obtained from SEM. Where possible, analysis of SEM images was also used to estimate porosity and its standard deviation at the end of an experiment for comparison with volume changes estimated from pore volumometry. However, this approach is subject to additional unquantifiable errors that can change the apparent porosity relative to that reported in Table 1. Increase in apparent porosity can occur through plucking of fine particles during cutting and grinding of recovered samples, or through problems of distinguishing talc (that normally crystallizes in pores) flakes from void space. Decrease in apparent porosity can occur if pores are small enough that backscattered contrast is generated from pore walls that lie below the plane of the polished surface, and when there is a large amount of olivine present the plateaux of polished olivine tend to stand higher than the interstitial softer phases, so that it can be difficult to distinguish the porosity from the softer matrix phases. Modes were determined from between 10 and 15 images for each sample.

3. Results

The 64 deformation experiments reported here are summarized in Table 1. Reproducibility was verified from several repeated tests. Experimental data are shown in Figs. 2–10.

Table 1
Details of experiments performed

Test#	Temp (°C)	Def'm Conf Press (MPa)	Def'm Eff. Press (MPa)	Log strain rate (s^{-1})	Porosity after dehydr. (% ± 0.5%)	Final porosity SEM (vol %)	Porosity change during Def'm (% ± 0.2%)	Yield stress (MPa ±5 Mpa)	Final stress (MPa ± 2 Mpa)	Final strain (% ± 0.2%)	Olivine (%)	Comments
Dry samples, no dehydration												
95	450	27	27	−3.6	–	–	–	356	–	–	–	Brittle
49	450	100	100	−3.6	–	–	–	336	–	2.2	–	Brittle
48	450	200	200	−3.6	–	–	–	266	270	2.2	–	Semi-brittle
Wet samples, no dehydration												
96	450	100	0	−3.6	–	–	–	154	150	0.8	–	Brittle
91	450	106	6	−3.6	–	–	–	181	52	8.4	–	Brittle
86	450	120	20	−3.6	–	–	–	220	235	5.0	–	Brittle
14	450	172	55	−3.6	–	–	–	220	254	2.8	–	Semi-brittle
13	450	198	94	−3.6	–	–	–	220	292	4.1	–	Semi-brittle
12	450	199	150	−3.6	–	–	–	220	291	4.2	–	Semi-brittle
Partial dehydration at 5 MPa effective pressure, except 78 and 80 dehydrated at 100 MPa.												
92	450	105	5	−3.6	–	3.7 ± 1.8	–	90	30		16.0 ± 6.5	Brittle (slow vol. leak)
78	450	120	20	−3.6	5.5	<0.5	+0.4	135	180	7.5	13.7 ± 3.6	Brittle
80	450	120	20	−3.6	4.5	1.8 ± 1.0	−0.7	125	155	8.5	3.2 ± 1.0	Brittle
64	450	200	49	−3.6	1.9	3.3 ± 1.1	−4.5	140	218[b]	3.4	6.4 ± 1.4	Semi-brittle
63	450	207	102	−3.6	5.4	3.0 ± 1.2	−2.7	145	255	5.0	15.2 ± 2.8	
62	450	202	150	−3.6	~2.6	1.4 ± 0.8	−0.4	150	322	5.3	4.3 ± 2.3	
Dehydration at 100 MPa effective pressure, deformed at 450 °C or deformed at dehydration temperature												
98[a]	570	130	30	−3.6	21.9	15.5 ± 4.4	−8.2	55	73.7	18.5	43.5 ± 3.3	
8[a]	570	160	50	−3.6	20.2	9.7 ± 2.1	−8.6	105	160[b]	17.1	41.2 ± 6.6	
18[a]	570	196	68	−3.6	17.1	9.7 ± 2.8	−9.6	102	193	18.2	42.7 ± 4.6	
16[a]	548	192	70	−3.6	21.7	15.6 ± 2.6	−8.2	105	203	12.6	36.0 ± 1.4	
17[a]	555	196	71	−3.6	20.7	11.1 ± 2.6	−7.4	110	195[b]	16.7	43.6 ± 4.2	
9[a]	555	175	82	−3.6	14.0	15.4 ± 5.8	–	115	203	6.6	27.0 ± 1.7	
37[a]	565	190	92	−3.6	16.0	6.0 ± 3.4	–	100	162[b]	13.7	29.8 ± 5.6	
59[a]	545	190	97	−3.6	17.1	7.9 ± 2.3	−4.8	120	252[b]	10.7	37.9 ± 7.0	
20[a]	562	200	99	−3.6	26.0	4.3 ± 1.1	−9.6	125	253[b]	14.1	46.4 ± 4.3	
97[a]	560	210	140	−3.6	21.9	3.0 ± 1.1	−22.0	95	259[b]	22.9	38.2 ± 7.2	
90	450	105	5.0	−3.6	23.1	6.8 ± 3.6	+0.3	101	40	6.1	37.3 ± 5.0	Brittle
71	450	154	56	−3.6	19.1	3.1 ± 1.3	−2.5	128	137	17.1	29.7 ± 4.6	
69	450	194	94	−3.6	21.0	10.8 ± 2.7	−5.4	135	214[b]	15.7	45.7 ± 7.3	
99	450	203	133	−3.6	~20	5.5 ± 1.1	-4.3	145	287[b]	22.5	46.7 ± 5.1	Vol. failure
70	450	200	146	−3.6	21.1	6.1 ± 3.8	−9.0	125	277[b]	17.5	49.3 ± 6.7	
94	450	230	185	−3.6	20.5	–	−18.0	25	379[b]	28.4	–	
83	450	222	180	−3.6	19.0	6.0 ± 2.1	−0.3	215	320	18.5	25.7 ± 7.0	Compact init. 180 MPa
Dehydration at 35 MPa effective pressure, 560 °C, deformed at 450 °C; or deformed at dehydration temperature												
75[a]	544	135	35	−6.05	–	1.2 ± 0.9	−14.2	62	148[b]	11.0	18.7 ± 5.2	Partial dehydr.
77[a]	533	135	35	−7.1	–	11.3 ± 2.8	–	20	75	9.6	40.6 ± 7.5	(Vol. Leak)
25[a]	563	120	20	−3.6	17.4	8.2 ± 3.6	–	50	72	6.1	40.2 ± 0.8	
22[a]	565	135	35	−3.6	14.6	–	−3.6	63	94	11.0	–	
21[a]	565	150	49	−3.6	21.5	11.7 ± 2.3	−10.8	66	155	17.2	43.9 ± 4.8	
19[a]	557	200	147	−3.6	14.3	14.7 ± 2.2	−9.6	15	263	16.6	49.5 ± 7.2	
93	450	150	5.0	−3.6	18.5	14.9 ± 4.8	–	40	41	4.5	39.6 ± 4.3	Brittle
74	450	103	21	−3.6	8.3	–	0	48	52	4.4	–	
87a	450	137	37	−3.5	18.8	–	−6.7	54	81	18.5	–	Initial loading
87b	450	137	37	−6.6	–	–	−7.4	18.2	–	20.5	–	Stress stepping, creep
87c	450	137	37	−6.25	–	–	−7.8	37.2	–	21.8	–	Stress stepping, creep

87d	450	137	37	−5.6	–	–	−8.1	74.5	–	22.4	–	Stress stepping, creep
87e	450	137	37	−5.3	–	12.8 ± 3.2	−10.1	101.7	–	23.6	42.7 ± 2.5	Stress stepping, creep
88a	450	180	80	−3.6	23.2	–	−6.5	45	147	9.9	–	Initial loading
88b	450	180	80	−6.8	–	–	−6.4	21.7	–	12.8	–	Stress stepping, creep
88c	450	180	80	−6.6	–	–	−6.5	45.5	–	12.9	–	Stress stepping, creep
88d	450	180	80	−6.1	–	–	−6.7	84.8	–	13.2	–	Stress stepping, creep
88e	450	180	80	−5.8	–	–	−6.9	118.8	–	13.5	–	Stress stepping, creep
88f	450	180	80	−5.6	–	–	−7.2	144	–	13.9	–	Stress stepping, creep
88 g	450	180	80	−5.4	–	5.3 ± 1.8	−7.5	165	–	14.5	42.7 ± 6.9	Stress stepping, creep
79	450	200	95	−3.6	~20	9.7 ± 2.9	–	18	166[b]	26.1	47.3 ± 4.6	
81	450	220	179	−3.6	18.1	2.7 ± 1.3	−6.3	122 h	–	–	35.5 ± 6.9	P[a] determination
89a	450	–	176	–	16.4	–	−6.9	115 h	–	–	41.5 ± 8.0	P[a] determination
89b	450	226	176	−3.6	–	3.4 ± 0.9	−14.7	50	301[b]	17.9	41.5 ± 8.0	
Dehydration at 5 MPa effective pressure, deformed at 450 °C; or deformed at dehydration temperature												
11[a]	547	190	92	−3.6	16.1	4.9 ± 1.4	−16	8	214	21.1	49.4 ± 4.0	
45[a]	553	190	96	−3.6	16.3	4.5 ± 2.1	−16	31	136	9.6	46.2 ± 7.8	
7[a]	570	176	98	−3.6	18.0	–	−18	47	268[b]	26.6	52.4 ± 2.6	
6[a]	573	193	109	−3.6	17.0	–	−16.8	25	266	25.5	34.1 ± 2.3	
76	450	120	20	−3.6	17.1	7.8 ± 3.5	−10.7	57	64[b]	38.5	40.0 ± 6.2	High ductile strain
67	450	182	35	−3.6	14.1	7.1 ± 1.8	−16.5	62	145[b]	29.9	35.5 ± 4.2	
84	450	135	35	−7.1	22.2	4.5 ± 2.2	–	25	126	13.3	39.5 ± 7.7	
82	450	135	35	−6.0	23.4	4.0 ± 2.3	−9.8	42	169	22.9	41.8 ± 5.3	
72	450	170	67	−3.6	18.9	–	−22.5	30	156[b]	29.5	–	
66	450	206	114	−3.6	19.2	7.8 ± 2.6	−15.8	40	270[b]	25.0	38.8 ± 5.7	
85a	450	–	123	–	20.4	7.5 ± 2.0/11.5	−10.6	84 h	–	–	46.7 ± 9.9	P[a] determination
85b	450	203	123	−3.6	–	–	−16.2	35	247[b]	25.1	–	
65	450	208	161	−3.6	16.2	8.4 ± 1.8	−4.0	120	308[b]	20.4	46.8 ± 7.6	
73	450	–	214	–	18.3	4.9 ± 2.9	−8.2	84 h	–	–	50.2 ± 8.2	P[a] determination
Talc deformation, dry									Stress at 10% strain			
Te5	554	200	200	−3.6	–	–	–	53	44[c]	7.5	–	
Te2	450	200	200	−3.6	–	–	–	64	74	15.6	–	
Te3	450	200	200	−3.6	–	–	–	64	74	12.5	–	
Te4	450	200	200	−6.6	–	–	–	56	75[c]	9.5	–	
Te6	440	70	35	−3.6	–	–	–	27	39[c]	1.6	–	Brittle
Te7	440	200	150	−3.6	–	–	–	50	66[c]	6.1	–	

Porosity change during deformation includes elastic volume reduction. All tests fully ductile except where stated in comments. Within groups samples are listed in order of increasing effective confining pressure. h = effective hydrostatic stress. Vol. = volumometer. Error values are standard errors for that particular specimen, and do not include variability within that group between different specimens; −ve porosity changes represent compaction.

[a] Deformed at dehydration temperature.

[b] Constant-volume flow attained.

[c] Extrapolated value.

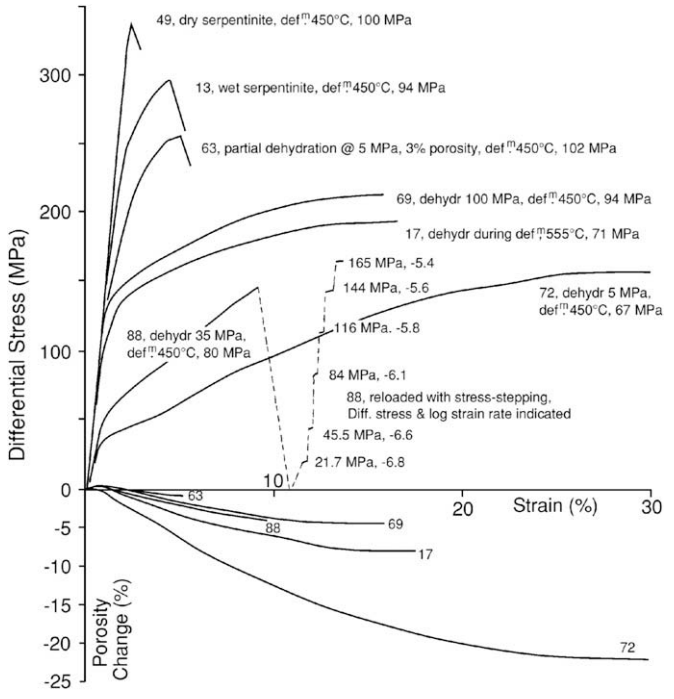

Fig. 2. Representative stress/strain and porosity change curves covering the range of conditions of experiments performed at a strain rate of $10^{-3.6}$ s^{-1}. Specimen numbers correspond to those in Table 1. Dehydration and deformation temperature and effective pressure conditions are given with each curve. The second part of test 88 is a stress-stepping test. Differential stress and log strain rate (−ve number) are given with each step.

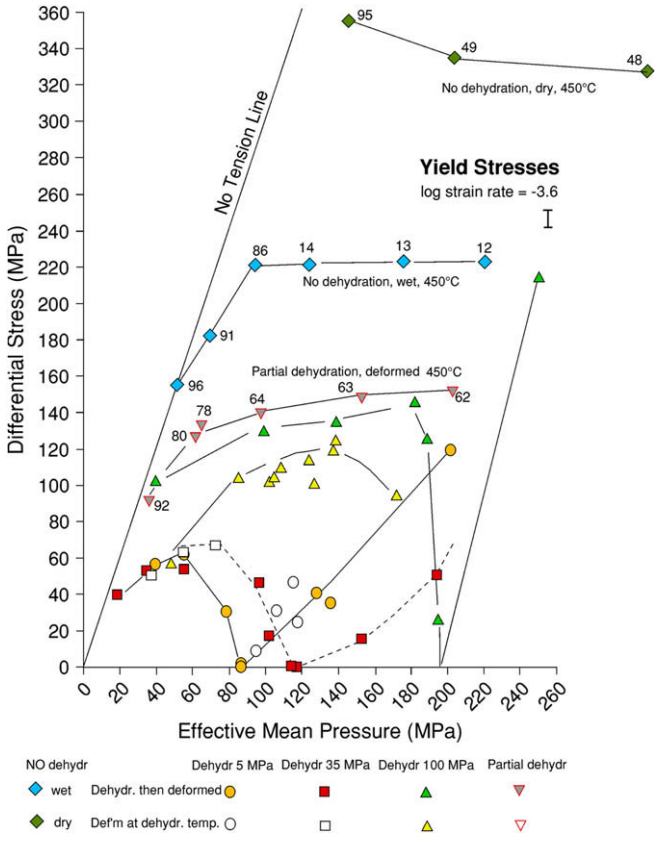

Fig. 3. Yield stress values (±5 MPa) for all tests performed at a strain rate of $10^{-3.6}$ s^{-1}. Specimen numbers corresponding to those given in Table 1 are shown for tests displaying the higher yield stresses. Test numbers corresponding to the lower yield stresses are shown on Fig. 6. Line segments link tests of the same temperature and dehydration conditions.

3.1. Dehydration reaction

From microstructural, element mapping and X-ray diffraction (XRD) observations the dehydration reaction was inferred to be

$$5\ \text{serpentine(lizardite)} = 6\ \text{forsterite} + 1\text{talc} + 9H_2O$$

From XRD and microstructural studies we observed no evidence of antigorite production in our run products.

The above reaction results in a solid phase volume of about 25% less than that of the parent serpentinite. Thus if it is carried out at zero effective confining pressure there is a corresponding increase in the porosity of the sample. Because at 'low' water pressures (up to 2 GPa) the Clapeyron slope of this reaction is positive, the volume of water generated in the reaction is greater than the new pore volume, and excess water must be expelled to maintain the pore pressure constant. In practice, the amount of porosity that could be created by complete dehydration was a little less than 25% because the specimens were not initially 100% serpentine. In addition, a small amount of undehydrated serpentine still remains in the samples even after long time periods.

The temperature for the onset of breakdown over the pressure range of these experiments (with pore pressure = confining pressure) was estimated for chrysotile serpentine (believed comparable in this respect to lizardite) to be ca. 450 °C at 250 MPa using THERMOCALC software (Holland and Powell, 1998). The precise breakdown temperature of lizardite is sensitive to solid solution effects, for example increasing markedly with aluminium content (Chernosky et al., 1988). We have not attempted to map out variations in Al-content in detail, but element maps and a number of microprobe analyses showed alumina contents heterogeneously distributed and ranging up to about 0.7 wt% that might lead to heterogenous dehydration at a given temperature. We have noted that serpentinite in veinlets and the grain boundary regions of

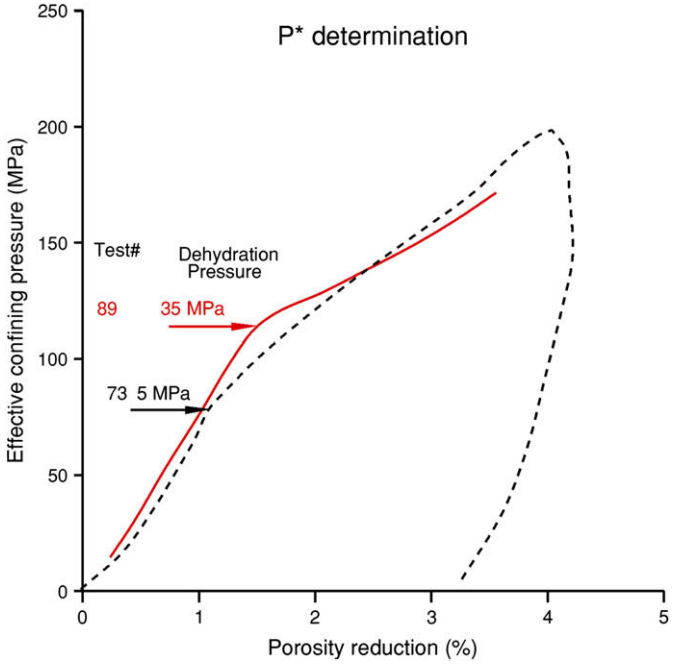

Fig. 4. Hydrostatic effective stress-path tests 73 (dashed line) and 89 (solid line) to determine the critical pressure (P^*) at 450 °C required for the onset of pore collapse in tests previously dehydrated at 560 °C at 5 MPa and 35 MPa effective pressures.

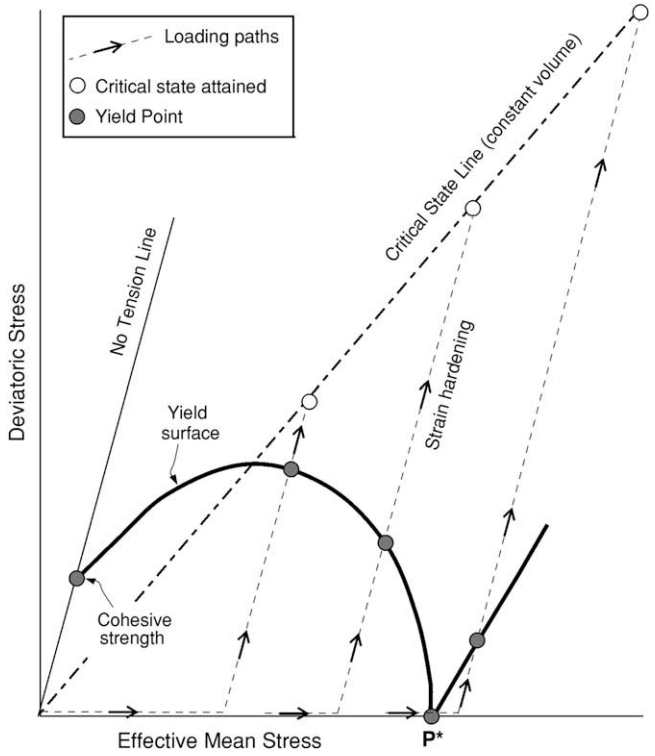

Fig. 5. Schematic illustration of expected mechanical behaviour of a porous material. The yield surface at low effective mean pressures represents dilatant deformation with brittle faulting and rises to a peak stress on the critical state line. Then it decreases in the region of shear-enhanced compaction until P^*, the effective hydrostatic pressure for pore collapse. At higher effective mean pressures the yield stress rises again. Various possible stress paths for axisymmetric shortening are shown. Post-yield behaviour involves strain-hardening, compactive ductile flow ending at the critical state line, where isovolumetric, steady flow occurs. The yield surface shrinks for materials of lower porosity.

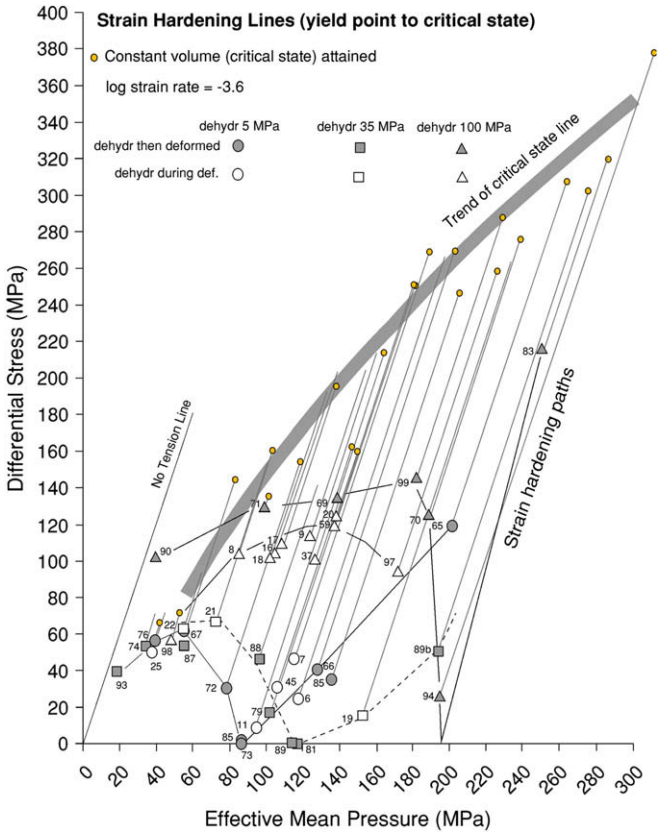

Fig. 6. Yield surface and strain-hardening pathways for serpentinite after total dehydration (all to ~20% porosity) at different effective confining pressures, showing correspondence with the critical state model of the deformation of porous rocks. The amplitude of the yield surface loop increases with increasing effective pressure during dehydration. Straight lines of slope 3 link yield stresses to the stress at which constant-volume flow is attained (small circular symbols). Strain-hardening flow develops along these lines that become longer at higher effective mean pressures. Strain-hardening lines not terminated with a small circle symbol did not attain constant volume, steady flow. The trend of the constant-volume (critical state) line appears to be approximately the same for tests with different histories. Specimen numbers shown with each plotted point correspond to those in Table 1.

pseudomorphed original olivine grains are most prone to dehydration.

The formation of small new grains of olivine was barely detectable even after long duration heat treatment at 520 °C, but reaction goes almost to completion (cessation of evolution of water) at 580 °C in a few hours. Thus these experiments employed oversteps in the range 70–130 °C relative to the estimated equilibrium temperature at a given pressure condition. Rates of dehydration observed in these experiments were statistically consistent with those reported by Llana-Fúnez et al. (2007), estimated using pore volumometry on samples from the same source at similar combinations of confining and pore fluid pressure. The onset of reaction could be detected at slightly lower temperatures, 500 °C, in powdered (Arkwright et al., 2008), faulted or sawcut samples (Rutter and Brodie, 1988). This is believed due to the pre-existence of drainage pathways and enhancement of reaction kinetics due to increased surface area and damage to grain surfaces. The kinetic data of Llana-Fúnez et al. (2007) for the solid samples allowed pre-estimation of the time required to bring about complete dehydration at a given temperature or amount of transformation likely during a deformation experiment of given duration and temperature.

3.2. Constant displacement rate tests prior to dehydration (at 450 °C)

To provide a standard of reference for samples deformed during or after deformation, several constant strain rate ($10^{-3.6}$ s^{-1}) tests were performed over a range of effective confining pressures up to 200 MPa on samples deformed both wet and dry at a temperature (450 °C) just below the onset of dehydration (Table 1 and Figs. 2 and 3). Samples tested dry are very strong, supporting differential stresses over 300 MPa and display brittle or semi-brittle behaviour, forming a sharply localized fault with little discernable crack damage away from the fault plane after only about 2% strain. There is hardly any dilatation prior to faulting and failure stress is insensitive to effective confining pressure. The presence of water (at a pore water pressure to keep the specimens wet) causes a substantial strength drop (~40% in yield strength, Figs. 2 and 3) and an increase in ductility. After initial positive strength sensitivity to pressure at low effective pressures (below 40 MPa), flow stress becomes pressure independent, with deformation at near-constant volume (cf. Escartín et al., 1997).

Some idea of strength sensitivity to large changes in strain rate was obtained from stress relaxation tests performed after an initial period of deformation at constant strain rate (wet tests 13 and 14).

3.3. Deformation experiments run after partial or complete dehydration at 450 °C at various effective hydrostatic pressures

Deformation experiments at constant strain rate ($10^{-3.6}$ s^{-1}) were run on samples after total or partial dehydration carried out at nominally 560 °C. Reaction progress was monitored by pore

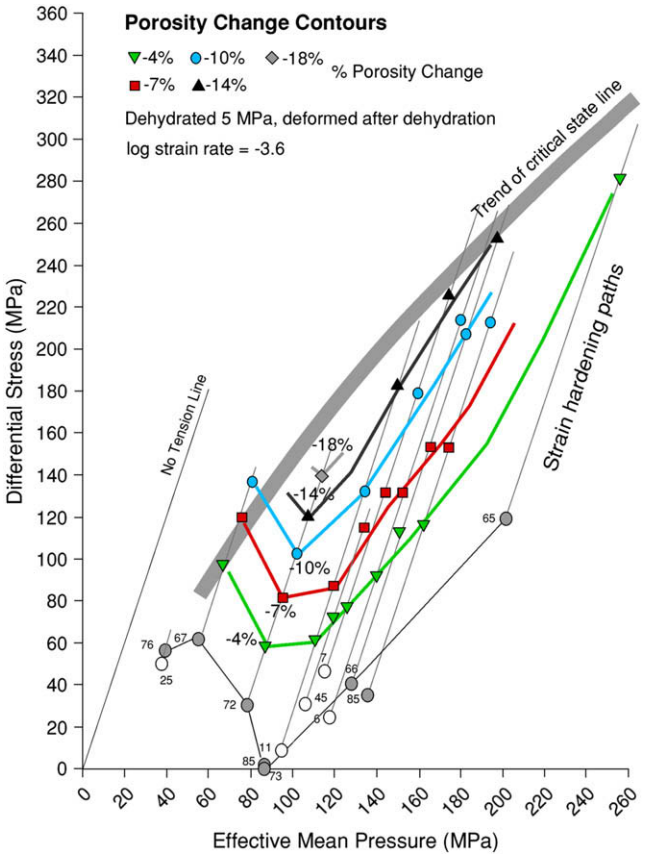

Fig. 7. Yield stress, strain-hardening paths and critical state line for samples dehydrated at 5 MPa, contoured for porosity evolution during strain-hardening flow. Porosity loss contours mirror the shape of the yield stress curve, with maximum porosity loss occurring in the region of shear-enhanced compaction. Sample numbers with each plotted yield point are as given in Table 1.

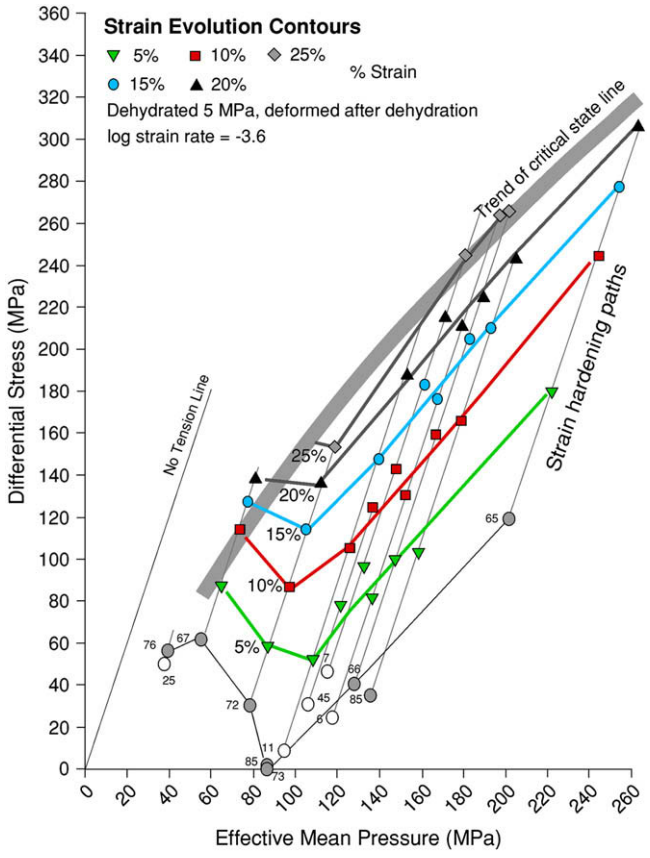

Fig. 8. Yield stress, strain-hardening paths and critical state line for samples dehydrated at 5 MPa, contoured for strain evolution during strain-hardening flow. Strain evolution contours mirror the shape of the yield stress curve, with maximum ductile strain occurring in the region of shear-enhanced compaction. Sample numbers with each plotted yield point are as given in Table 1.

volumometry. Specimens that were totally dehydrated were maintained at temperature until water expulsion ceased (after about 24 h). Temperature was then lowered to 450 °C for the deformation stage, further to ensure that the reaction was stopped. Partially dehydrated specimens were maintained at 560 °C until up to one-third the maximum amount of water had been expelled (about 6 h), whereupon temperature was rapidly lowered to 450 °C.

Total dehydration was carried out under 3 different effective pressures, nominally 100 MPa, 35 MPa and 5 MPa. A lowest effective pressure greater than 0 MPa has to be applied to ensure the copper jacket is firmly pressed against the specimen, thereby ensuring measured volume changes can arise only from generation or collapse of pore spaces within the specimen volume. Partial dehydration (resulting in a smaller porosity and lesser quantities of reaction products) was carried out at both 100 and 5 MPa effective pressure.

Yield stress for a stress/strain curve displaying ductile behaviour was taken to be the point of maximum curvature, which generally corresponded quite well with the onset of permanent volumetric compaction (Fig. 2). Because there is some subjective judgement involved in making this measurement, an uncertainty of ±5 MPa has been ascribed to the yield stress measurements (Fig. 3). Fig. 3 shows yield stresses for specimens pre-treated as above, and Fig. 2 shows the form of stress/strain data for a representative range of tests. At low effective confining pressures (less than 30 MPa) samples were brittle and deformed by shear faulting. At higher effective pressures, samples were ductile under all conditions, with marked strain-hardening following yield. Stress/strain curves for samples 69, 88, and 72, shown in Fig. 2, are typical of those deformed at the effective confining pressures indicated, respectively, after dehydration at nominal 100, 35 and 5 MPa effective pressures. At the higher effective pressures the post-yield strain-hardening can persist for 20% shortening or more, whereupon it gives way eventually to flow at constant differential stress (e.g. samples 69, 17 and 72 in Fig. 2). In some cases this constant-stress flow was terminated by faulting and stress drop after a few percent of strain. Corresponding volumometer data (Fig. 2) show that the strain-hardening is accompanied by volume reduction due to pore collapse, and the attainment of flow at constant differential stress corresponds to flow at constant volume. Thus the initial hardening is likely to be due to the pore collapse.

It was anticipated that porous, fully dehydrated samples would display yield by pore collapse under a critical hydrostatic effective pressure P^*. It is typical of porous solids that they possess a yield point under effective hydrostatic pressure. This pressure was measured during hydrostatic loading to high effective pressures (Table 1 and Figs. 3 and 4), and is clearly higher for samples dehydrated at higher effective pressures, even though the porosity after dehydration was the same. P^* for samples dehydrated at 5 MPa effective pressure is 85 MPa, 120 MPa for samples dehydrated at 35 MPa effective pressure and not less than 200 MPa for samples dehydrated at 100 MPa.

For uniaxially symmetric shortening experiments, stress paths on a plot of differential stress versus effective mean pressure $\sigma'/3 + (\sigma_c - P_p)$, where P_p is pore fluid pressure, σ_c is total confining

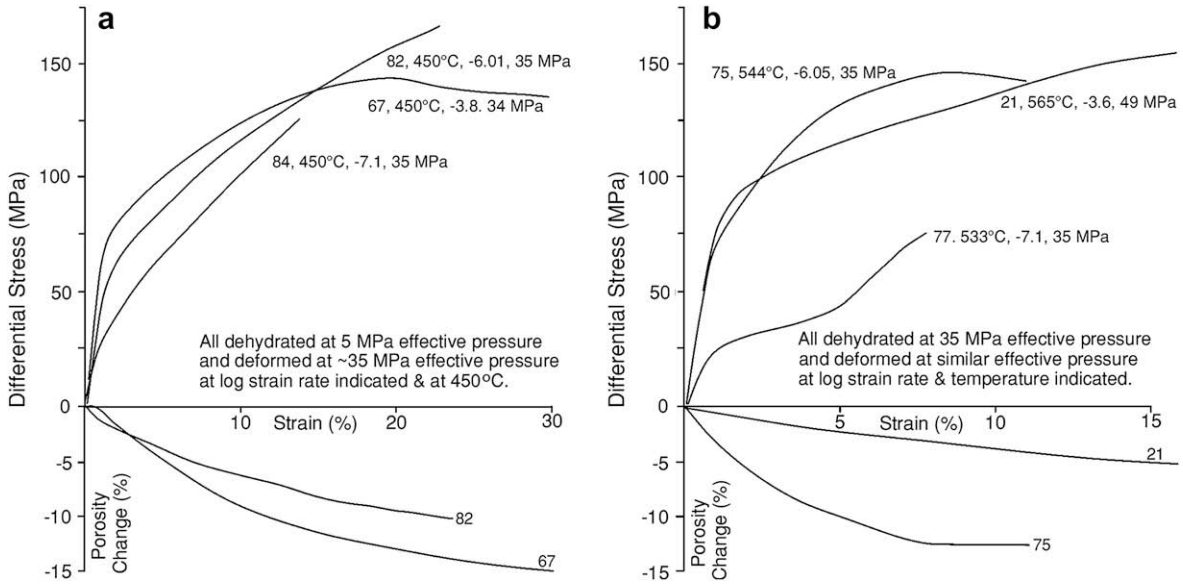

Fig. 9. (a) Stress vs strain and porosity vs strain curves (where available) for samples fully dehydrated at 560 °C, 5 MPa effective pressure then deformed at different strain rates at ~35 MPa effective pressure. Yield stress is reduced markedly by decreasing strain rate but at higher strains the difference is largely removed by the effects of strain-hardening. (b) Stress vs strain and porosity vs strain curves (where available) for samples deformed at 35 MPa effective pressure and at different strain rates and temperatures such that deformation and dehydration proceed together. In (a) and (b) with each curve is shown the sample number, deformation temperature, log strain rate (s^{-1}) (−ve number), and deformation effective confining pressure.

pressure and σ' is differential stress, have a slope of 3. All compressive stress states are confined to the right of a line through the origin of slope 3 (No Tension Line, Fig. 5). Thus post-yield strain-hardening history must lie on a line of slope 3 extending upwards from the yield point until either constant-stress flow is attained or failure with fault localization and stress drop supervenes. Fig. 6 shows yield stresses, strain-hardening stress paths and the attainment of constant-volume flow at the upper ends of the stress paths for the samples dehydrated at 5 MPa. Also shown in Figs. 7 and 8 are contours for the attainment of particular levels of axial strain and also volumetric strain (=porosity loss%). This pattern of behaviour is the same for all sets of tests, and the position of the constant-volume curve appears not to depend on the previous dehydration history. The contour patterns for axial and volumetric

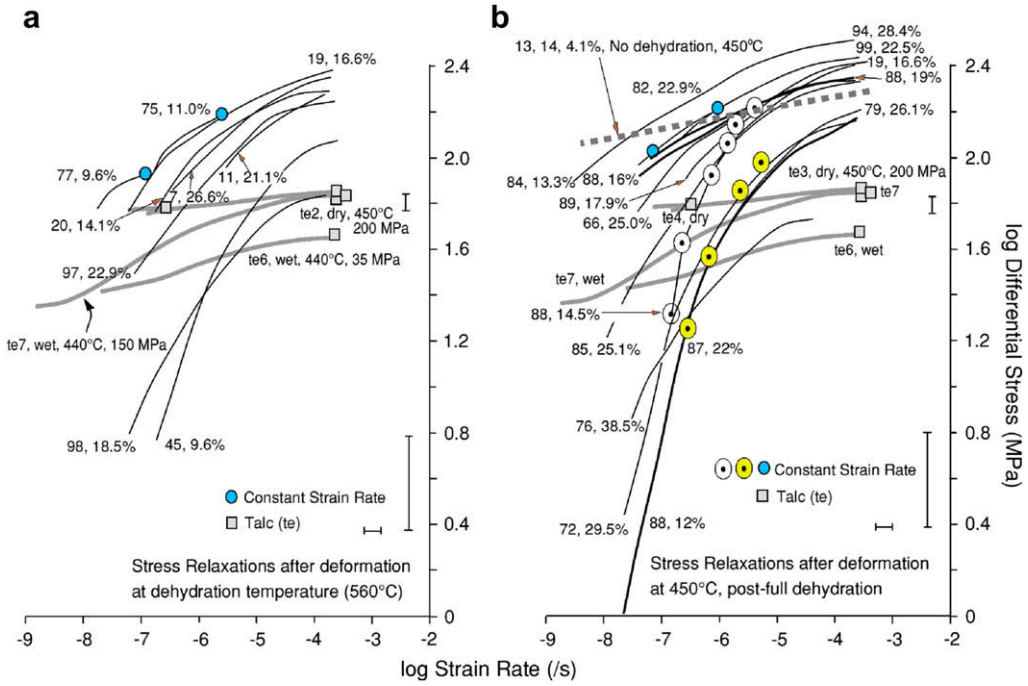

Fig. 10. Stress relaxation and stress-stepping tests to show rate sensitivity to strength in specimens deformed (a) at the temperature of dehydration and (b) after lowering the temperature to 450 °C. Amounts of permanent strain (%) at which each test was performed are indicated. Specimen numbers correspond to those in Table 1. All tests show tendency to increasing sensitivity of strength to strain rate, approaching linear viscous at low stresses. Both figures show data for wet and dry solid talc (small squares for flow stress at constant strain rate with continuous thick lines for stress relaxation behaviour) that demonstrate the relative lack of strength sensitivity to strain rate compared to dehydrated serpentinite. Data for tests 13 and 14 (thick dashed curve) show the relative lack of stress sensitivity to strain rate for non-dehydrated serpentinite at 450 °C.

strains during the strain-hardening history are similar to each other and also to the general shape of the yield point curve. Maximum axial and volumetric strains are attained on stress paths that start at effective pressures just below P^*, and the most rapid rates of strain-hardening are in tests that start from effective pressures above P^*. The constant-volume phase is attained at progressively higher differential stresses for deformation at higher effective confining pressures (Fig. 5).

During the strain-hardening phase at any instant the axial shortening strain (Fig. 8) is slightly more than the volumetric strain (Fig. 7). The contribution of the volumetric strain to axial shortening, however, is likely to be much less than the amount of the volumetric strain (about one-third the volumetric strain if the volume loss was to be isotropic). Thus the enhancement of the deformability in the axial direction as a result of porosity creation is much greater than can be explained solely by the volume change contribution to axial strain, and implies that the capacity for porosity reduction also enhances the accumulation of distortional strain.

Surprisingly, the effective pressure during dehydration strongly affects the subsequent mechanical behaviour, despite the post-dehydration porosity being the same in all cases. Samples dehydrated at 100 MPa effective pressure consistently display higher yield stresses and lower rates of strain-hardening than those dehydrated at 35 MPa. Correspondingly, samples dehydrated at 5 MPa effective pressure showed the lowest yield strengths and the longest periods of post-yield strain-hardening (Figs. 3 and 6) prior to the attainment of constant-volume flow. There was no distinction to be made between the yield strengths for samples deformed at the dehydration temperature (560 °C) and at 450 °C for 5 MPa and 35 MPa nominal dehydration effective pressures, despite the difference in temperature (Fig. 3). On the other hand, for samples dehydrated at 100 MPa nominal effective pressure, those deformed at 560 °C were slightly weaker than those deformed at 450 °C (Fig. 3).

For samples deformed at effective hydrostatic pressures less than P^*, the yield stress curve rises to a maximum at low effective pressures, then decreases toward P^* at higher effective pressures. Some samples were deformed at pressures higher than P^* (Fig. 3). After a yield strength minimum at P^*, yield stress rises again at higher effective pressures, after which some degree of porosity reduction has occurred, causing strengthening. For such samples, long intervals of post-yield strain-hardening occur prior to the attainment of constant-stress, constant-volume flow (Fig. 6).

Specimens that were partially dehydrated (at 5 MPa or 100 MPa effective pressure, post-dehydration porosity in the range 2–6%, and few reaction products) were consistently stronger (higher yield strengths) than those completely dehydrated (post-dehydration porosity ~20%, little serpentinite remaining, mineralogy dominated by olivine and talc) (Figs. 2 and 3). This comparison demonstrates the role of porosity in controlling the strength. Effective pressure during dehydration has no discernable effect on the strength of these samples, although this inference is based on relatively few experimental runs (Table 1).

In all cases the strength of the wholly or partially dehydrated serpentinite is markedly reduced relative to that of even wet, non-dehydrated serpentinite at the same (450 °C) temperature (Fig. 2).

3.4. Sensitivity of flow stress to deformation rate

The influence of deformation rate was explored (a) by means of a small number of constant strain rate experiments carried out over a range of strain rates between $10^{-3.6}\,s^{-1}$ and $10^{-7.1}\,s^{-1}$, (b) by terminating a number of constant strain rate tests with stress relaxation, and (c) by means of strain rate-stepping or stress-stepping tests during the course of deformation of a single specimen (e.g. specimen 88, Fig. 2); (b) and (c) have the advantage that the influence of specimen variability is eliminated, and some idea of rheological characteristics can be obtained from an experiment on a single sample. In the case of stress relaxation tests (Rutter et al., 1978), after some amount of permanent strain, the motor drive is switched off and the time-dependent decay of differential stress with time is observed, as stored elastic energy in the machine plus specimen is dissipated through permanent strain in the sample. Knowing the elastic stiffnesses of the latter, stress relaxation curves can be recast as plots of differential stress vs instantaneous strain rate. The total permanent strain accumulated during a stress relaxation is typically 1–2%. Similar amounts of strain were allowed during the course of stress-stepping tests to minimise the amount of strain-hardening during the course of the test.

Constant strain rate tests over a range of strain rates were performed (i) on specimens dehydrated fully at 5 MPa effective pressure after reducing temperature to 450 °C, and (ii) on specimens deformed and dehydrated at 35 MPa (or nearby) effective pressure at combinations of strain rate and temperature such that a substantial amount of the total dehydration would take place during the course of the deformation (Fig. 9 and Table 1). Thus lower strain rate tests were carried out at lower temperatures in the overall temperature range 570–533 °C. Such 'synmetamorphic deformation' tests can be compared to those in which the deformation was carried out after the reaction had been completed or arrested.

In both cases, (i) and (ii), reducing the strain rate substantially reduces the yield stress, but this difference is progressively offset at higher strains by the effects of strain-hardening. In (i) the deformation begins after full porosity has been produced under hydrostatic stress. In (ii) porosity is progressively generated during the deformation, and collapsed as it is formed. A comparison of Fig. 9a and b shows that, in broad terms, similar rheological characteristics result, hence synmetamorphic deformation may enhance deformability even though the transient porosity may be small.

Fig. 10 shows the combined results of all three types of test on serpentinite samples both deformed after dehydration and cooling to 450 °C and deformed at the dehydration temperature but after completion of the reaction. Because these experiments all display strain-hardening associated with pore collapse, and the instantaneous flow stress varies according to effective pressure during dehydration, the accumulated strain, the porosity, and the stress level from which a stress relaxation curve begins can be highly variable. Thus the present dataset is not sufficiently extensive to provide a basis for estimation of a constitutive flow law, which would have to involve both strain and porosity as parameters, but several general observations can be made from them:

(a) with decreasing strain rate, the stress sensitivity to strain rate approaches linear viscous. This applies to the results of stress relaxation, strain rate-stepping and stress-stepping experiments for the dehydrated specimens (Fig. 10),
(b) the higher the starting stress level for a stress relaxation curve, the lower the strain rate at which linear-viscous behaviour is approached,
(c) rapid weakening at low strain rates is a characteristic only of specimens dehydrated or dehydrating. Samples deformed at 450 °C without dehydration remain relatively strong even at low strain rates (e.g. samples 13 and 14, Fig. 10).

3.5. Mechanical behaviour of solid talc specimens

Experiments were run on cylinders of dry talc, at 450 and 550 °C, 200 MPa total confining pressure and at strain rates ranging between $10^{-4}\,s^{-1}$ and $10^{-7}\,s^{-1}$ (Figs. 10 and 11). Wet tests were run

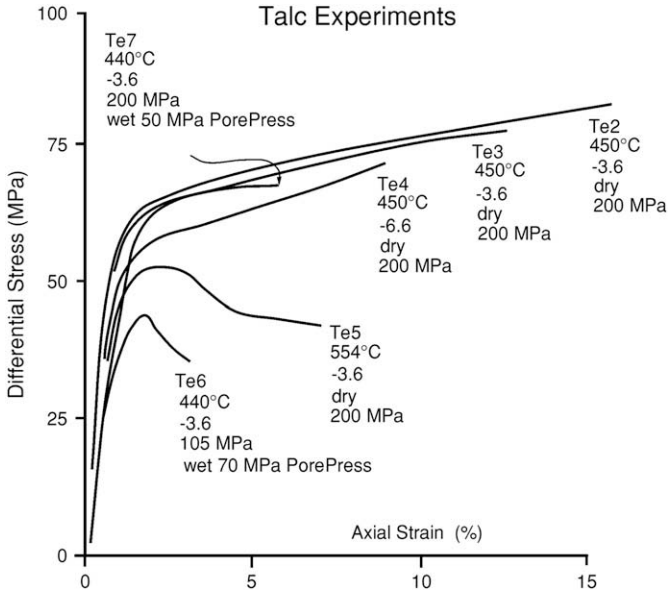

Fig. 11. Summary of stress–strain data from experiments on solid cylinders of talc at 440, 450 and 554 °C over a range of effective pressures that correspond to those for several serpentinite experiments. Total and pore pressures and log strain rates (−ve numbers) are indicated. Specimen numbers correspond to Table 1. At high effective pressures talc shows sharp yield and gently strain-hardening ductile flow. The presence of water does not affect behaviour. There is some weakening and loss of ductility associated with 100 °C temperature rise or at a lower effective confining pressure (35 MPa).

at 440 °C with effective pressures of 150 MPa and 35 MPa, the latter to be comparable to test conditions for many serpentinite experiments (Table 1). At the higher effective pressures talc showed uniform ductility except that at strains about 10% ill-defined localization of a wide fault zone began to form. At 35 MPa effective pressure the talc faulted after only a small strain. Stress–strain curves show a fairly constant flow stress of ca. 70 MPa at 450 °C with slight strain-hardening. These results are consistent with those reported for talc rocks by Escartín et al. (2008). Strength decreases slightly with temperature increase from 450 to 554 °C, but the wet sample at 150 MPa effective pressure is apparently not weaker than the dry material at comparable effective pressure. Wet talc tested at 35 MPa effective pressure was about one-third weaker than when tested at higher effective pressures, and less ductile. Pore volumometric measurements showed no apparent volumetric strain under any test condition. Dry talc strength is almost completely insensitive to large variations in strain rate (Fig. 10). The wet talc showed greater weakening at low strain rates, but strength remains still relatively insensitive to strain rate compared to dehydrating or dehydrated serpentinite.

3.6. Microstructures

Fig. 1b shows the appearance of sample 63, partially dehydrated at 560 °C, to produce about 15% volume of uniformly dispersed new olivine grains. Fig. 1c–f shows the appearance of samples almost fully dehydrated at different effective pressures. In samples dehydrated at only 5 MPa effective pressure (Fig. 1c, sample 6), new olivine forms uniformly distributed both within and around serpentine grains. Fig. 1d shows the relationship at high magnification of new olivine grains (~10 μm diameter) surrounded by talc and pore space. Talc flakes occupy new pore spaces and can be recognized from their randomly oriented, platy habit. When they are compacted through pore space collapse they are hard to discern owing to their similar electron backscatter coefficient to serpentine, hence it is easy to underestimate the quantity present. At 100 MPa dehydration pressure (Fig. 1e, specimen 16), and at 35 MPa (Fig. 1f, specimen 77) new grains of olivine typically form in clusters of grains about 10 μm wide, and develop preferentially around lizardite grain boundaries that pseudomorph orginal olivine grains, thereby forming contiguous 'cages' of olivine grains. New olivine also forms preferentially along serpentine veinlets that formed along pre-existing cracks. In all cases, no collapse of newly generated porosity accompanied dehydration, hence the new porosity is the same. Approximately 80 MPa, 120 MPa and 200 MPa effective pressure, respectively, is required to initiate pore collapse in samples dehydrated at each of the three (5, 35 and 100 MPa) dehydration pressures. We might expect this marked contrast in strength to be reflected in microstructural differences.

Although all of the specimens whose microstructures are shown in Fig. 1 have been deformed by up to 25% shortening, they tend to show no microstructural indication of how this was accomplished. There is no evidence of pervasive cataclasis nor of plastic flattening of olivine grains. On the other hand, suitably oriented (cleavage parallel to compression direction) enclosed grains of chlorite often reveal substantial amounts of strain through the development of kink bands (Fig. 12a and b), implying that the surrounding granular clusters of olivine have undergone relative displacements. At higher magnification in the SEM and using TEM the new olivine 'grains' that are on the order of 10 μm across are seen to be internally heterogeneous and microstructurally polygranular. They have complex internal structures, with growth zoning (Fig. 12c) and development of extensive patches, sometimes microporous, of ultrafine-grained (200 nm) olivine (Fig. 12d).

4. Discussion

4.1. Experimental data

4.1.1. Effect of dehydration pressure on yield strength

We attribute the higher yield strength of serpentinite dehydrated at high effective pressures to the formation of 'cage' structures of new olivine grains around old serpentine grain boundaries (Fig. 1e and f). These structures presumably require the observed higher hydrostatic and/or differential stresses to force them to compact. We infer that dehydration becomes relatively suppressed within serpentinite grain interiors and focused around grain boundaries at high effective pressures because it is harder to form new, connected drainage networks leading from olivine nuclei forming in serpentinite grain interiors than around the edges or in veinlets. Development and maintenance of locally higher pore fluid pressures around intragranular nuclei than the pore pressure around well-drained olivine nuclei at grain edges means that intragranular nuclei have a smaller thermal overstep and hence are kinetically disadvantaged. At lower effective pressures, it should be easier to drain the interior of serpentinite grains, leading to the formation of more scattered nucleation, and hence the failure to develop the stronger cellular structure. However, whilst this difference between samples dehydrated at 5 MPa compared to all higher effective pressures is easy to perceive, the microstructural differences between the 35 MPa and 100 MPa dehydrated samples are not so clear, given the significant differences in strength they display.

4.1.2. Interpretation of mechanical behaviour

Rutter and Brodie (1995) suggested that when a metamorphic reaction results in a reduction of solid phase volume so that new porosity is generated, the principles of critical state soil mechanics (e.g. Muir Wood, 1991) might be used to help understand the resulting changes in mechanical properties. Here we have demonstrated that this is broadly true for dehydrated serpentinite

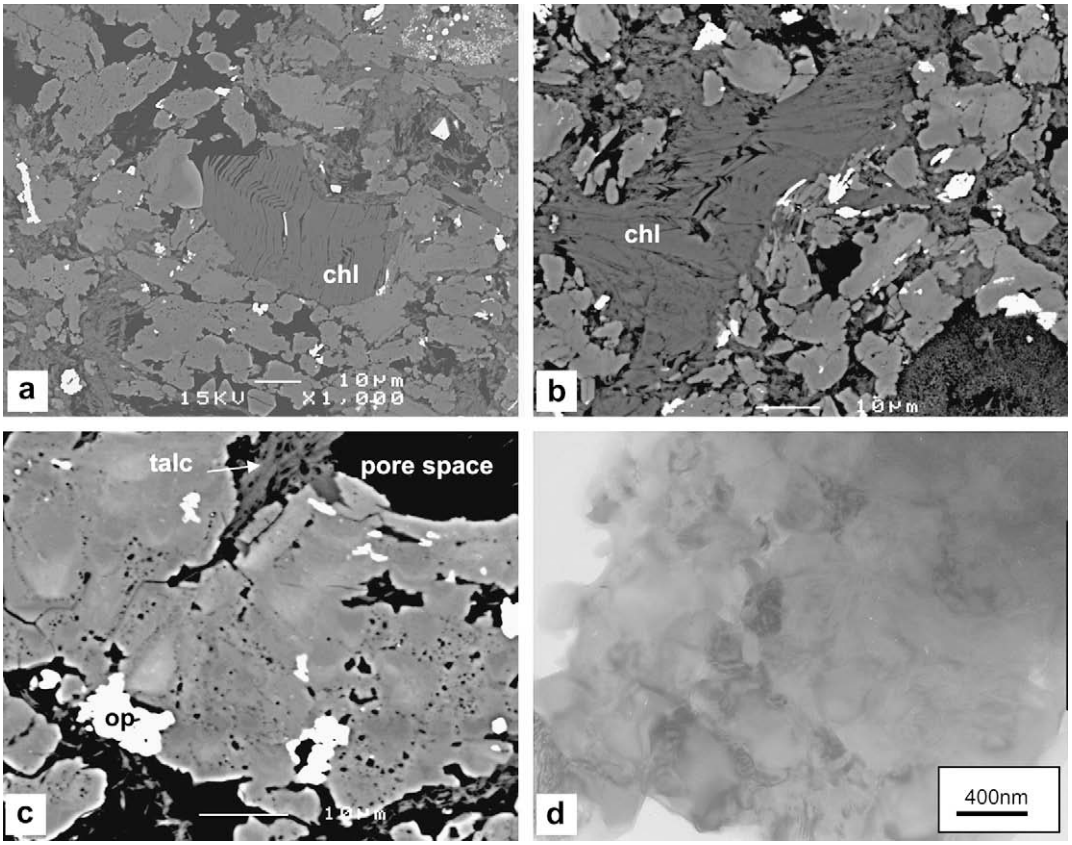

Fig. 12. SEM Backscattered electron micrographs showing: (a) and (b) chlorite grains (chl) showing crenulation due to shortening of the sample (compression direction vertical) but little evidence of deformation within surrounding olivine aggregates. (c) Syton-polished sample showing fine structure and porosity within olivine grains. (d) TEM micrograph showing the ultrafine-grained substructure developed within olivine aggregates.

which, like a soil or weak rock, is a fluid-saturated porous solid, with the following characteristics. Comparing the partially dehydrated (less-porous) rock with the fully dehydrated samples, the former is stronger and more prone to brittle failure. The latter shows high degrees of ductility with capped yield surface behaviour, a peak yield stress separating regimes of localized brittle faulting at low effective pressures from ductile flow involving shear-enhanced compaction at higher effective pressures. For samples taken at effective pressures beyond P^* before application of differential load, yield stress begins to rise again as the rock shows strengthening associated with decreasing porosity. In the ductile flow regime, post-yield behaviour is characterized by rapid strain-hardening with pore collapse, eventually attaining flow at constant differential stress and constant volume (critical state). The stress required to attain critical state increases rapidly with increasing confining pressure, and its value seems to be independent of the pathway (stress-path and dehydration history) by which it is reached.

In two respects the mechanical behaviour of serpentinite differs from that of porous rocks at low temperatures:

(a) Even for the same amount of porosity generation, dehydrated serpentinite displays a higher yield strength when dehydrated at higher effective pressures. This means that there is no simple relation between strength and porosity. The same porosity can be represented by different microstructural configurations that result in different levels of cohesive strength.
(b) The higher temperature means that the dehydrated serpentinite can display strength characteristics that are temperature and time sensitive. The relative lack of sensitivity of the strength of serpentinite (prior to dehydration) to strain rate is illustrated by stress relaxation data for samples 13 and 14 (Fig. 10). At low strain rates the serpentinite can retain high strength whilst the dehydrated rock (at the same temperature or higher) cannot. This demonstrates unequivocally that dramatic weakening is associated with the dehydration reaction.

4.1.3. Deformation mechanisms

Microstructural observations suggest that ductile deformation of the dehydrated or dehydrating serpentinite involves relative displacements between and/or within clusters of olivine grains – granular flow – that is essential to bring about the observed compaction of pores space during deformation. That the olivine grains, apparently ~10 μm across, contain a heterogeneous substructure of ultrafine (200 nm, Fig. 12), defect-free grains and microporosity corresponds to our previous findings (Rutter and Brodie, 1988), in which sliding occurred on fault planes (previously induced or sawcuts) that became decorated with ultrafine-grained olivine during the dehydration reaction. It was inferred that, despite the low temperature, such ultrafine olivine could deform by diffusion-accommodated grain boundary sliding. Then and now, this inference was supported by a rheological transition with decreasing strain rate to linear-viscous flow (Fig. 10).

Talc is also a volumetrically significant product of the dehydration reaction. We present mechanical data for samples of zero-porosity talc (Figs. 10 and 11). Although it is a relatively weak sheet silicate mineral, it is strong compared to dehydrating serpentinite at low strain rates and displays a completely different stress

sensitivity to strain rate. Furthermore, the microstructural arrangement of talc grains, in randomly oriented aggregates between a structural framework of olivine grains, and a lack of formation of areas of contiguous, oriented talc in shear zones, suggest that significant load is not normally transferred to the talc, although they may facilitate granular flow of olivine grain clusters.

4.2. Geological implications

4.2.1. Comparative strengths of olivine and serpentinite rocks

At a temperature of ca. 500 °C olivine-dominated rocks are expected to be very strong (provided the grain size is not ultrafine) compared to serpentinite (Hirth and Kohlstedt, 2003; Drury, 2005) at geological strain rates. Hilairet et al. (2007) argued that, except at temperatures high enough for dehydration to begin, serpentinite is likely to be the weakest phase deforming by intracrystalline plastic flow, and hence that serpentinized upper mantle will localize creep deformation in a subducting slab beneath the depth range of shallow earthquakes. Extrapolating the trend of our stress relaxation data for wet but non-dehydrated lizardite serpentinite to low strain rates ($\sim 10^{-14}\ s^{-1}$) suggests that it may be able to sustain stresses not higher than about 80 MPa (but not as low as suggested by Hilairet et al., 2007).

Lizardite is the serpentine phase typically produced in the hydration of oceanic lithospheric mantle rocks. During heating and pressurization in a subduction zone it seems likely that it may recrystallize to antigorite plus brucite before the temperature of lizardite dehydration is reached (Wicks and O'Hanley, 1988; Yang and Powell, 2008). This recrystallization is known to be sluggish under experimental conditions (Chernosky et al., 1988), which presumably explains why we did not find any in our run products. From high strain rate experiments, antigorite serpentinite appears to be about 30% stronger for fracture and flow than lizardite under comparable conditions (Raleigh and Paterson, 1967; Escartín et al., 1997). Hence the fracture/flow behaviour of serpentinites in nature prior to dehydration is likely to be affected by the possibility of this transformation during prograde metamorphism. Presently, the effects of large changes in strain rate on the strength and ductility of serpentinite phases are not well known. The characteristic microstructural differences between lizardite (pseudomorphous after original peridotite texture) and antigorite (bladed, interpenetrating texture produced by solid-state metamorphic recrystallization) may also influence the microstructural evolution during the dehydration reaction and, as we have found with lizardite, affect the mechanical strength. Antigorite begins to dehydrate at temperatures on the order of 50–60 °C higher than lizardite, and brucite dehydration in the same temperature range also contributes to the total fluid flux budget.

4.2.2. Mechanical effects of the dehydration reaction

During prograde metamorphism of a subducting slab, water is likely to be released from a series of dehydration reactions involving serpentinite in stages beginning at ca. 65 km depth (1.7 GPa and 460 °C) and ending with complete serpentinite dehydration at ca. 100 km (3 GPa and 620 °C) (Yang and Powell, 2008). Other phases (e.g. chlorite) or Al- or Ca-rich serpentinites extend the dehydration interval to greater depths. Yang and Powell (2008) present evidence, from a garnet peridotite inferred to have been produced during subduction of sub-oceanic mantle, of relicts of lizardite armoured by olivine. These imply that lizardite can sometimes persist metastably to high pressures and eventually dehydrate. Thus serpentinite-related dehydration in the subduction environment cannot be portrayed simply in terms of the breakdown of a single phase at a particular pressure/temperature condition. This complexity must be borne in mind when considering the application of experimental rock mechanics data to deformation in a subduction zone.

Raleigh and Paterson (1967) suggested that brittle deformation might result from the undrained (evolved water unable to escape) dehydration of serpentinite (and other hydrous phases) in the lithospheric mantle, leading to the reduction of effective overburden pressure, and that this might explain the occurrence of intermediate depth (50–300 km) earthquakes in subduction zones. Dobson et al. (2002) showed that serpentinite dehydration under high pressures (1.5–8.5 GPa) is accompanied by microseismic emissions, indicating that dilatant fracturing events are indeed possible despite the high imposed pressure. Jung et al. (2004) similarly demonstrated deformation by faulting during dehydration under the same range of pressures. It has been common to assume that the locus of dehydration reactions in subduction zones also corresponds to the locus of seismicity, from the early work of Raleigh and Paterson (1967) through to more recent work (e.g. Seno et al., 2001).

Dehydration/deformation experiments are generally carried out at high strain rates under isothermal conditions and most commonly are undrained, so that evolved water under pressure cannot escape. Under these conditions brittle failure of the test piece is inevitable. Dehydration reactions are endothermic, so that the overall rate is controlled by the heat flux. Hence in nature, evolution of water may not take place rapidly enough to cause catastrophic failure of the dehydrating rock if the system is drained. Generation of porosity enhances permeability (Tenthorey and Cox, 2003; Llana-Fúnez et al., 2007), which will facilitate drainage. Additionally, as we have shown here, the progression of the dehydration reaction also leads to rapid relaxation of deviatoric stress on the rock mass, inhibiting brittle failure in the serpentinite itself.

Although brittle failure of the serpentinite might be inhibited by these effects, it may conversely be enhanced in the surrounding, non-dehydrating peridotites and metagabbroic rocks, which will find themselves subjected to reduced effective overburden pressure from the local supply of pressurized water. Further, formation of a local volume of dehydrating serpentinite in which deviatoric stress is relaxed may cause lateral transfer of load to the surrounding rocks, further increasing their potential for seismogenic failure. Thus we suggest that to assume a direct correlation of observed loci of seismicity with the actual sites of dehydration reactions might represent an oversimplification.

For experiments such as those reported here, carried out at low total pressures, where the Clapeyron slope of the dehydration reaction is positive, the volume of water generated exceeds the pore space created as a result of the decrease in solid phase volume. This situation may arise in transform fault zones if serpentinite is dehydrated through heat arising from displacement against the end of the adjacent ridge segment (e.g. Rutter and Brodie, 1987). The excess fluid volume must be dissipated either by hydraulic fracturing or via the enhanced permeability that accompanies porosity generation and reduction in effective pressure (Brace et al., 1968). Whilst high pore pressure may inhibit pore compaction, it will not prevent the relaxation of non-hydrostatic stresses, which can take place by intergranular sliding even at near-constant porosity. The excess fluid production and its migration may influence the localization of transform-related seismicity.

At the much higher pressures within subduction zones, the Clapeyron slope of dehydration reactions is negative (e.g. Jung et al., 2004), and the volume of water produced is smaller than the potential porosity created. But the resultant effective confining pressure will rapidly drive pore collapse, ensuring that the evolved water becomes pressurized. Relaxation of differential stress and fluid drainage should therefore take place in the same way that we observe in our lower total pressure experiments.

4.2.3. Deformation/metamorphism interactions

It is widely held that much deformation in orogenic belts is accompanied by prograde metamorphic reactions, commonly involving dehydration. Little is known of such deformation/metamorphism interactions from naturally deformed rocks because in nature the syntectonic microstructure is generally overprinted by the effect of higher temperature microstructural equilibration and mimetic grain coarsening under conditions of relaxed differential stress. The behaviour of serpentinite observed here helps to indicate the potential complexity of deformation/metamorphism interactions, which can involve the effects of generation of pressurized fluid (if undrained), the effects of transient generation of ultrafine-grained reaction products and the transient mechanical weakening effects arising from the generation of collapsible porosity.

A particular note of caution is required when attempting to infer likely mechanical behaviour of rocks dehydrating under geological conditions, based on observations from much faster laboratory experiments. Experimental dehydration must be carried out with a substantial temperature overstep, so that the reaction can take place in a short period of time. Large oversteps typically lead to high densities of reaction product nucleation points in the microstructure relative to rates of grain growth, such as we see in our experiments (e.g. Fig. 1b and c). A natural example of dehydration of serpentinite under hydrostatic stress conditions (i.e. with no accompanying deformation) is provided by the contact metamorphic aureole around the Bergell granitoid in the Western Alps (Trommsdorff and Evans, 1972; Mellini et al., 1987). Because the reaction is endothermic, once the pore pressure rises to a steady value or becomes equal to the lithostatic pressure, the overall rate of progression is controlled by the conductive heat flux. Walther and Wood (1984) argued that dehydration reactions in nature proceed with only a small ($<10\,^{\circ}C$) overstep, and this is reflected in the Bergell aureole by the growth of large (1–4 mm) olivine crystals mantled by talc, and separated by even larger distances from neighbouring olivines. Such a microstructural evolution would no doubt result in a different evolution of mechanical properties than we see in experiments. On the other hand, *syntectonic* dehydration may result in less striking microstructural differences. Localized shearing during the progression of the reaction seems to enhance nucleation rates and favour the production of fine-grained reaction products in experiments (Rutter and Brodie, 1988), and this is supported by observations of syntectonic dehydration of serpentinite from the Voltri massif, Italy (Hoogerduijn-Strating and Vissers, 1991; Hermann et al., 2000).

5. Conclusions

Intact cylinders of serpentinite were deformed experimentally at confining pressures of up to 250 MPa and over a temperature range 450–560 °C, encompassing the range of the dehydration reaction to olivine + talc + water. Pore volumometry was used to track porosity changes arising from the dehydration reaction and from pore collapse during deformation. Serpentinite deformed dry is strong and brittle at these temperature/pressure conditions. The presence of water causes reduction of yield stress by ca. 40%. Deformation mode remains brittle but lack of volume change during deformation results in no sensitivity of strength to effective confining pressure.

Samples were fully dehydrated to induce generation of ca. 20% porosity. This resulted in marked further reduction of yield stress to an amount that was greater for dehydration under higher effective pressures. The pattern of mechanical behaviour was identical to that of porous weak rocks or soils at low temperatures, characterized by a yield cap and a critical hydrostatic pressure for yield by pore collapse. Yield was followed by strain-hardening accompanied by porosity reduction and eventual attainment of critical state – deformation at constant volume at constant flow stress. The critical state line is approximately independent of the stress path by which it is attained. Post-yield strain-hardening was greater for deformation at higher effective pressures.

Flow stresses in dehydrated samples are strongly sensitive to strain rate, more so as strain rate is reduced, eventually displaying linear viscosity. In contrast, non-dehydrated serpentinite remains strong at low strain rates. Microstructural study showed deformation to involve granular flow without cataclasis and without intracrystalline plastic flow of the olivine. Granular flow leading to pore collapse and ductility is inferred to be facilitated through the deformation of clusters of ultrafine grain-sized olivine (200 nm) produced during the dehydration reaction. The higher yield stresses found for specimens dehydrated at higher effective pressures seems to arise from the formation of contiguous ‘cells’ of load-bearing olivine.

Provided similar microstructures are produced in naturally deformed serpentinites, such as in subduction zones or transform fault zones, serpentinite should tend to relax shear stresses, transferring load and expelled pressurized water laterally into stronger, non-dehydrated rocks that will become more likely to fail seismogenically.

Acknowledgements

This work was performed with the support of UK Natural Environment Research Council grant NER/A/S/2003/00305. Experimental Officer Robert Holloway is thanked for help with the construction and maintenance of experimental equipment. This work was completed whilst E.H.R. was in receipt of grant support from the Spanish Ministry of Education and Science during sabbatical leave at the Institute of Earth Sciences “Jaume Almera” in Barcelona (CSIC).

References

Arkwright, J.C., Rutter, E.H., Brodie, K.H., Llana-Fúnez, S., 2008. Role of porosity and dehydration reaction on the deformation of hot-pressed serpentinite aggregates. Journal of the Geological Society 165, 639–649.

Brace, W.F., Walsh, J.B., Frangos, W.T., 1968. Permeability of granite under high pressure. Journal of Geophysical Research 73, 2225–2236.

Chernosky, J.V., Berman, R.G., Bryndzia, L.T., 1988. Stability, phase relations and thermodynamic propertie of chlorite and serpentine group minerals. In: Ribbe, P.H. (Ed.), Reviews in Mineralogy, vol. 19, pp. 295–346.

Dobson, D.P., Meredith, P.G., Boon, S.A., 2002. Simulation of subduction zone seismicity by dehydration of serpentine. Science 298, 1407–1410, doi:10.1126/science.1075390.

Drury, M.R., 2005. Dynamic recrystallization and strain softening of olivine aggregates in the laboratory and the lithosphere. Special Publication of the Geological Society of London 243, 143–158.

Escartín, J., Hirth, G., Evans, B., 1997. Non-dilatant brittle deformation of serpentinites: implications for Mohr–Coulomb theory and the strength of faults. Journal of Geophysical Research 102, 2897–2913.

Escartín, J., Andreani, M., Hirth, G., Evans, B., 2008. Relationships between the microstructural evolution and the rheology of talc at elevated pressures and temperatures. Earth and Planetary Science Letters 268, 463–475, doi:10.1016/j.epsl.2008.02.004.

Hermann, J., Muntener, O., Scambelluri, M., 2000. The importance of serpentinite mylonites for subduction and exhumation of oceanic crust. Tectonophysics 327, 225–238.

Hilairet, N., Reynard, B., Wang, Y., Daniel, I., Merkel, S., Nishiyama, N., Petitgirard, S., 2007. High pressure creep of serpentine, interseismic deformation, and initiation of subduction. Science 318, 1910–1913.

Hirose, T., Bystricky, M., Kunze, K., Stünitz, H., 2006. Semi-brittle flow during dehydration of lizardite-chrysotile serpentinite deformed in torsion: implication for the rheology of oceanic lithosphere. Earth and Planetary Science Letters 249, 484–493.

Hirth, G., Kohlstedt, D.L., 2003. Rheology of the upper mantle and the mantle wedge. In: Eiler, J. (Ed.), Inside the Subduction Factory. Geophysical Monograph, vol. 138, pp. 83–185.

Hoogerduijn-Strating, E.H., Vissers, R.L.M., 1991. Dehydration-induced fracturing of eclogite-facies peridotites – implications for the mechanical-behavior of subducting oceanic lithosphere. Tectonophysics 200, 187–198.

Holland, T.J.B., Powell, R., 1998. An internally consistent thermodynamic data set for phases of petrological interest. Journal of Metamorphic Geology 16, 309–343.

Jung, H.H., Green, H.W., Dobrzhinetskaya, L.F., 2004. Intermediate depth earthquake faulting by dehydration embrittlement with negative volume change. Nature 428, 545–549.
Llana-Fúnez, S., Brodie, K.H., Rutter, E.H., Arkwright, J.C., 2007. Experimental dehydration kinetics of serpentinite using pore volumometry. Journal of Metamorphic Geology 25, 423–428.
Mellini, M., Trommsdorff, V., Compagnoni, R., 1987. Antigorite polysomatism: behaviour during progressive metamorphism. Contributions to Mineralogy and Petrology 97, 147–155.
Miller, S.A., Van Der Zee, W., Olgaard, D.L., Connelly, J.A., 2003. Fluid pressure feedback model of dehydration reactions: experiments, modelling and application to subduction zones. Tectonophysics 370, 241–251.
Muir Wood, D., 1991. Soil Behaviour and Critical State Soil Mechanics. Cambridge University Press. 486pp.
Olgaard, D.L., Ko, S.C., Wong, T.F., 1995. Deformation and pore pressure in dehydrating gypsum under transiently drained conditions. Tectonophysics 245, 237–248.
Poirier, J.P., 1982. On transformation plasticity. Journal of Geophysical Research 87, 6791–6797.
de Ronde, A.A., Stünitz, H., Tullis, J., Heilbronner, R., 2005. Reaction-induced weakening in experimentally deformed plagioclase-olivine aggregates. Tectonophysics 409, 85–106.
Raleigh, C.B., Paterson, M.S., 1967. Experimental deformation of serpentinite and its tectonic implications. Journal of Geophysical Research 70, 3965–3985.
Renner, J., Viskupic, K., Hirth, G., Evans, B., 2003. Melt extraction from partially molten peridotite. Geochemistry, Geophysics, Geosystems 4, 8086–9007, doi:10.1029/2002GC000369.
Rutter, E.H., Atkinson, B.K., Mainprice, D.H., 1978. On the use of the stress relaxation testing technique in studies of the mechanical behaviour of geological materials. Geophysical Journal of the Royal Astronomical Society 55, 155–170.
Rutter, E.H., Brodie, K.H., 1987. On the mechanics of oceanic transform faults. Annales Tectonica 1, 87–96.
Rutter, E.H., Brodie, K.H., 1988. Experimental 'syntectonic' dehydration of serpentinite under controlled pore water pressure. Journal of Geophysical Research 93, 4907–4932.
Rutter, E.H., Brodie, K.H., 1995. Mechanistic interactions between deformation and metamorphism. Geological Journal 30, 27–240.
Rutter, E.H., Brodie, K.H., 2004. Experimental intracrystalline plastic flow in hot-pressed synthetic quartzites prepared from Brazilian quartz crystals. Journal of Structural Geology 26, 2011–2023.
Seno, T., Zhao, D., Kobayashi, Y., Nakamura, M., 2001. Dehydration of serpentinized mantle slab: seismic evidence from southwest Japan. Earth, Planets and Space 53, 861–871.
Tenthorey, E., Cox, S.F., 2003. Reaction-enhanced permeability during serpentinite dehydration. Geology 31, 921–924.
Trommsdorff, V., Evans, B.W., 1972. Progressive metamorphism of antigorite schist in the Bergell tonalite aureole (Italy). American Journal of Science 272, 423–437.
Walther, J.V., Wood, B.J., 1984. Rate and mechanism in prograde metamorphism. Contributions to Mineralogy and Petrology 88, 246–259.
Wicks, F.J., O'Hanley, D.S., 1988. Serpentine minerals: structure and petrology. In: Ribbe, P.H. (Ed.), Reviews in Mineralogy, vol. 19, pp. 91–168.
Yang, J.-J., Powell, R., 2008. Ultrahigh pressure garnet peridotites from the devolatilization of sea-floor hydrated ultramafic rocks. Journal of Metamorphic Geology 26, 695–716, doi:10.1111/j.1525-1314.2008.00780.x.